The birth of a bubble: A molecular simulation study

Alexander V. Neimark[a] and Aleksey Vishnyakov
Center for Modeling and Characterization of Nanoporous Materials, TRI/Princeton, Princeton, New Jersey 08542

(Received 24 August 2004; accepted 13 October 2004; published online 21 January 2005)

We study the nucleation of a bubble in a metastable Lennard-Jones (LJ) fluid, confined to a spherical pore with wetting walls, by a combination of grand canonical, canonical ensemble, and gauge cell Monte Carlo simulation methods complemented by the Voronoi–Delaunay tessellation analysis of statistical geometry of intermolecular cavities. We construct the isotherm of confined fluid in the form of a continuous van der Waals' loop, in which the unstable backward trajectory between the spinodals corresponds to bubble states. We show that as the degree of metastability increases and the fluid becomes progressively stretched, the decrease of fluid density is associated with the evolution of a population of interstitial intermolecular cavities. At the spinodal, the fluid becomes mechanically unstable: Interstitial cavities partly coalesce into a larger cavity located due to the system symmetry around the pore center. This cavity represents a bubble embryo, which grows at the expense of interstitial cavities. The nucleation barrier is calculated by direct thermodynamic integration along the isotherm. We compare our simulation results to the predictions of the classical nucleation theory and experiments on capillary condensation–evaporation of nitrogen in pores of hybrid organic–inorganic mesoporous molecular sieve HMM-3. [DOI: 10.1063/1.1829040]

I. INTRODUCTION

Spontaneous formation of bubbles in metastable liquids, known as cavitation, plays a critical role in various technological and natural phenomena which involve liquid–vapor phase transformations. Cavitation may occur either in a superheated liquid at a temperature higher than its boiling temperature at given pressure or in a stretched liquid at a pressure lower that the saturation pressure at given temperature.[1,2] In most cases, such as cavitation erosion of propellers and turbines[3,4] or explosive boiling of cryogenic liquids,[5] this role is negative. In other cases, such as sonoluminescence[6] or ultrasonic cleaning,[7,8] cavitation is useful. Despite its ubiquity, the physical mechanisms of bubble nucleation are still incompletely understood, hindering reliable predictions of the rates of nucleation and the attainable conditions of liquid superheating and stretching at given environmental conditions. Starting from Gibbs,[9] bubble formation as the initial stage of liquid–vapor phase transitions has been a subject of enduring interest to theoreticians and engineers. Recent advances in molecular simulations and statistical mechanics of inhomogeneous fluids have triggered a new wave in studies of nucleation phenomena in general and bubble formation in particular on a molecular level.[10–23]

When a metastable liquid does not contain impurities or solid surfaces, which may catalyze heterogeneous nucleation, formation of bubbles is a fluctuation driven process. A qualitative scenario of homogeneous nucleation is described by the classical nucleation theory (CNT).[9,24,25] Thermal fluctuations in local configurations of molecules cause emerging small, nanometer sized voids, which serve as bubble embryos. According to statistical mechanics, the probability of observation of a bubble embryo of size r is determined by the reversible work required for its formation $W(r)$. In order to survive and to give birth to a bubble, which then would grow spontaneously, an embryo must exceed some critical size. Smaller embryos collapse. Critically sized embryos are called critical nuclei. Their size, r_{cr}, is determined from the condition of maximum of the work of formation, $W'(r)|_{r=r_{cr}}=0$, that is well understood: The growth of a critical nucleus leads to the gain in the free energy of the system as a whole. Assuming a spherical shape of bubble embryos, the work of its formation is given by[9]

$$W(r)=4\pi r^2\gamma-\tfrac{4}{3}\pi r^3(P_V-P_l). \tag{1}$$

Here, γ is the vapor–liquid interfacial tension, P_l and P_v are the liquid and vapor pressures, respectively. The size of critical nuclei corresponding to the maximum $W(r)$ is given by

$$r=2\gamma/(P_v-P_l). \tag{2}$$

This relation is the Laplace equation of mechanical equilibrium for a spherical interface. Thus, the nucleation barrier, which equals the work of formation of the critical nucleus, is proportional to the radius squared

$$W(r)=\tfrac{4}{3}\pi r^2\gamma. \tag{3}$$

From the thermodynamic standpoint $W(r)$ represents the difference of the grand thermodynamic potentials of a fixed volume V of the liquid with the bubble, $\Omega_b=-(V-\frac{4}{3}\pi r^3)P_l-\frac{4}{3}\pi r^3P_v+4\pi r^2\gamma$, and without, $\Omega_l=-VP_l$, at the given chemical potential μ and temperature T

[a]Author to whom correspondence should be addressed. Electronic mail: aneimark@triprinceton.org

$$W(r) = \Omega_b(\mu, V, T) - \Omega_l(\mu, V, T). \quad (4)$$

Although the contribution of the system volume V cancels out in the classical scheme of Gibbs[9] [Eqs. (1)–(3)], Eq. (4) in which V is contained explicitly, has a general character. Equation (4) is applicable for nucleation in small volumes where the system volume V may affect the nucleation. Recalling the Gibbs equation, $\partial\Omega/\partial\mu|_{V,T} = -N$ (N is the number of molecules in the system at given μ, V, T), we come from Eq. (4) to the nucleation theorem,[24,25] which relates the nucleation barrier to the excess mass of the nucleus

$$N_{\mathrm{ex}} = N_d(\mu, V, T) - N_v(\mu, V, T), \quad (5)$$

in the form

$$\partial W/\partial\mu|_{V,T} = -N_{\mathrm{ex}}. \quad (6)$$

The excess mass of the nucleus, N_{ex}, is negative. Within the framework of CNT, it is equal to

$$N_{\mathrm{ex}} = -\tfrac{4}{3}\pi r^3(\rho_l - \rho_v), \quad (7)$$

where ρ_l and ρ_v are the densities of the metastable liquid and stable vapor bulk phases at the given μ and T. Equation (7) defines the bubble equimolar radius.

Critical nuclei are inherently unstable. They correspond to the local maxima of the grand thermodynamic potential with respect to density variations. Thus, to study the nucleation in a metastable fluid one has to trace thermodynamically metastable and labile states. This can be done by imposing certain constraints on density fluctuations. In macroscopic thermodynamic models and mean-field approximations, such as the density functional theory, the constraints are enforced explicitly. In molecular simulations, the states of interest can be stabilized by restricting, in one way or another, the sampling in order to avoid their spontaneous destruction. Typically, the nuclei are modeled in a close system at the conditions of the canonical ensemble (e.g., Ref. 26) or generated in an open system at the conditions of the grand canonical or isothermal–isobaric ensembles using the umbrella sampling and configuration bias techniques.[27,28]

In this paper, we study the nucleation of a bubble in a metastable LJ fluid confined in a spherical pore with wetting walls by a combination of grand canonical ensemble (GCMC), canonical ensemble (CEMC) and gauge cell MC simulation methods. This model system provides ideal conditions to follow an elementary act of homogeneous nucleation in a quasi-equilibrium fashion. The small size of the system does not allow for the formation of more then one nucleus. The attractive potential exerted by the pore walls impedes heterogeneous nucleation and facilitates bubble formation in the pore center. The finite volume of the system makes it possible to simulate the system as a whole without any artificial boundary conditions, such as constraints of spatial periodicity introduced in simulations of ''infinite'' systems. Most importantly, bubble cavitation in stretched fluids confined to nanoscale pores of spheroidal shape can be studied experimentally with high precision using ordered mesoporous molecular sieves of cagelike pore structure.[29–31]

The paper is structured as follows: In Sec. II, we generate the MC isotherm of capillary condensation and evaporation of a LJ fluid in a spherical pore of 15.8 molecular diameters in width. The fluid–fluid and fluid–solid parameters were chosen to mimic nitrogen in silica pores at the nitrogen boiling temperature of 77.4 K. The GCMC isotherm constructed without imposing any constraints on the system exhibits a prominent hysteresis loop with vertical steps corresponding to spontaneous condensation and evaporation. The gauge cell method,[32,33] in which the level of density fluctuations is controlled, allowed us to complement the abrupt GCMC isotherm with a continuous trajectory of metastable and labile states in the form of a van der Waals' loop. The region of achievable metastability of the confined fluid was extended up to the very spinodals. The constructed isotherm corresponds to equilibrium in the canonical ensemble for a close system immersed in the thermal bath. The backward branch of the labile states corresponds to critical bubbles, which would be unstable in an open system. The nucleation barriers are calculated as the difference of the grand thermodynamic potentials, Eq. (4), by the integration along the continuous isotherm. The nucleation barriers for nanoscale bubbles are found to be appreciably smaller than the predictions of the classical nucleation theory.

In Sec. III, we apply the Voronoi–Delaunay tessellation technique (see Refs. 34–37) to study the statistical geometry of intermolecular cavities in the metastable liquid. For a given configuration of molecules, a cavity is defined as a connected region where there is sufficient space to accommodate an additional molecule. The geometrical analysis of molecular configurations helps understand the physical scenario of cavitation. We show that as the degree of metastability increases, the decrease of fluid density is associated with the evolution of a population of interstitial intermolecular cavities in the stretched fluid. At the spinodal the fluid becomes mechanically unstable: Interstitial cavities partly coalesce into a larger cavity located due to the system symmetry around the pore center. This cavity represents a bubble embryo, which grows at the expense of interstitial cavities into a critical nucleus; there with the fluid around the growing bubble consolidates. At the same time, the volume distribution of interstitial cavities remains self-similar. The surface-to-volume ratio for interstitial cavities over the seven orders of magnitude obeys the three-dimensional scaling, $S \sim V^{2/3}$.

In Sec. IV, we compare our simulation results with available experimental data on nitrogen sorption on ordered mesoporous molecular sieves of HMM-3 type with Pm3n cubic symmetry and make some conclusions. The experimental isotherm in spheroidal pores with the averaged diameter of 5.54 nm (15.8 molecular diameters) is reversible, in contrast to the GCMC simulated isotherm. Nevertheless, the experimental isotherm agrees quantitatively with the unconstrained equilibrium MC isotherm, which would be obtained in infinitely long GCMC simulation. That is, the nucleation barrier of about 30 kT, which was determined for the system under consideration here, is too large to be gotten through in our unbiased GCMC simulations of several million simulation steps. At the same time, this barrier is easily overcome in real experiments with characteristic equilibration time of several minutes and inherent fluctuations of environmental conditions, temperature and pressure.

Finally, the results are summarized briefly in Sec. V. We conclude that although the effects of confinement in the model system we considered here are not by any means negligible and the interaction with solid walls represents an additional stabilizing factor, we assume that the observed scenario of bubble formation via coalescence of interstitial cavities captures major features of homogeneous nucleation. Another outcome of this work is a better understanding of the origin of capillary condensation hysteresis observed in mesoporous materials.

II. MC SIMULATION OF BUBBLE FORMATION IN CONFINED LJ FLUID

A. Simulation details

We consider equilibrium configurations of a LJ fluid in a spherical pore of 16 molecular diameters in width with attractive LJ walls. The interaction parameters were chosen to mimic nitrogen at its normal boiling temperature of 77.4 K within a pore typical for silica mesoporous molecular sieves of cagelike structure. The LJ parameters for nitrogen were $\sigma=0.361\,54$ nm and $\epsilon/k=101.5$ K. The solid–fluid interactions were represented by the integrated LJ potential induced by the structureless spherical layer of oxygen atoms with solid–fluid parameters $\rho_s\epsilon_{sf}/k=2253\,\mathrm{K/nm^2}$, $\sigma_{sf}=0.317$ nm (ρ_s is the surface density of attractive centers). This model was employed in a series of our earlier works on modeling capillary condensation in cylindrical and spherical mesopores.[38] It was shown to provide excellent agreement with experimental data on mesoporous molecular sieves. The pore size of 15.8σ, or 5.54 nm, corresponds to the average ''internal'' pore diameter of a sample of HMM-3 material with Pm3n cubic symmetry.[39] This system was recently considered in Ref. 40 where we studied mechanisms of capillary condensation in ink-bottle pores. For detailed description of fluid–fluid and fluid–solid potentials and simulation protocols see Ref. 41.

Simulations were performed in different statistico-mechanical ensembles, which imply different constraints on the equilibrium states generated. We used a combination of the grand canonical ensemble (GCMC), canonical ensemble (CEMC) and gauge cell MC simulation methods. The standard Metropolis algorithm[42] was employed with simulation runs up to 15 million MC steps per molecule. Each step included one attempt of a molecule displacement in each cell, and two attempts of molecule removal, insertion, or transfer between the cells (when applicable). The maximum number of molecules was about 1400.

B. GCMC simulation

First, we performed GCMC simulation,[43] which does not enforce any constraints on the density fluctuations. The systems is considered in equilibrium with an infinite reservoir of bulk vapor thus mimicking experimental conditions of adsorption measurements. The GCMC isotherm is given in Fig. 1. It represents the average density in the pore as a function of the chemical potential μ, or, equivalently, the vapor pressure in the bulk reservoir. The isotherm exhibits a prominent hysteresis: Closed diamonds correspond to the adsorption

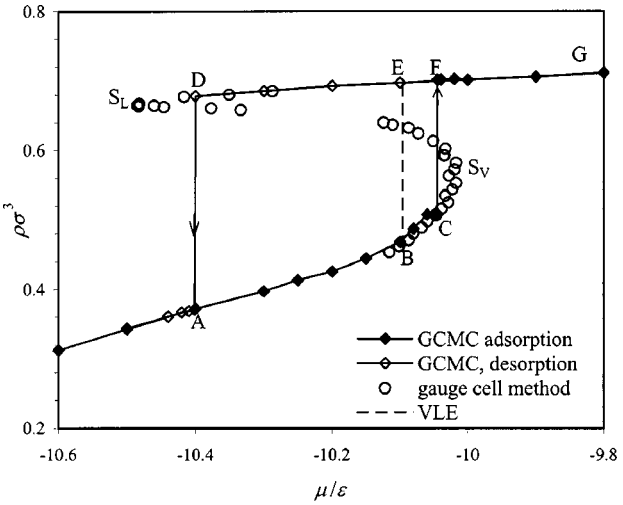

FIG. 1. MC isotherm of LJ fluid at $kT/\epsilon=0.762$ confined to a spherical pore of 15.8σ in diameter. B—vaporlike state at vapor–liquid equilibrium (VLE), C—limit of stability of vaporlike phase in GCMC method (fluid undergoes spontaneous capillary condensation transition to point F), S_V—vaporlike spinodal, S_L—liquidlike spinodal, D—limit of stability of liquidlike phase in GCMC method (fluid undergoes spontaneous evaporation transition to point A), E—liquidlike state at VLE, G—stable liquidlike state.

(condensation) branch obtained in a series of consecutive simulations with a monotonically increasing chemical potential μ (or vapor pressure) in which the last configuration generated at μ_i serves as the initial configuration for the next run at $\mu_{i+1}>\mu_i$ As the vapor pressure increases, the fluid in the pore forms a dense, adsorbed film at the wall, from submonolayer to monomolecular coverage to polymolecular layer. These configurations can be considered as shrinking bubbles surrounded by the growing adsorbed film dubbed as vaporlike states. A step-wise transition from a low density vaporlike state ($\rho=0.507\sigma^{-3}$) at point C $\mu=-10.046\epsilon$, to a high density liquidlike state ($\rho=0.701\sigma^{-3}$) at point F reflects spontaneous capillary condensation. The whole pore is filled by liquidlike fluid, which consolidates as the chemical potential increases further. Open diamonds correspond to the desorption (evaporation) branch obtained as the chemical potential decreases. These configurations correspond to liquidlike states. Spontaneous evaporation occurred at a lower chemical potential than that of spontaneous condensation. It is manifested by the step-wise transition from point D to point A at $\mu=-10.40\epsilon$, from $\rho=0.678$ to $0.371\sigma^{-3}$.

The hysteretic GCMC isotherm is qualitatively similar to experimental hysteretic isotherms observed in somewhat larger pores.[29,31] The hysteresis manifested in GCMC simulation shows that despite no constraints were in effect during the course of simulation, the sampling was confined either to the domain of low-density states or to the domain of high-density states. The energy barrier between these domains was too high to be overcome within a finite simulation run. If the simulation run were infinite and sampling included the whole configuration space, the isotherm would be reversible with a step BE located at the vapor–liquid equilibrium (VLE). Due to the finite size of the system this step should be somewhat rounded. However, for energy barriers exceeding several kT, this theoretical roundness is not perceptible. The would-be

reversible isotherm ABEG can be dubbed as the "true" GCMC isotherm in contrast with the "practical" hysteretic isotherm ACFGDA. The position of VLE in the pore is shifted as compared to the bulk VLE to a lower chemical potential, μ_e, which can be determined from the condition of equality of the grand thermodynamic potentials in the vaporlike and liquid states

$$\Omega_v(\mu_e,V,T)=\Omega_l(\mu_e,V,T), \tag{8}$$

which are defined through the Helmholtz free energies $F(N,V,T)$ of the vaporlike and liquidlike phases, respectively, as

$$\begin{aligned}\Omega_v(\mu,V,T)&=F(N_v(\mu),V,T)-\mu N_v(\mu),\\ \Omega_l(\mu,V,T)&=F(N_l(\mu),V,T)-\mu N_v(\mu).\end{aligned} \tag{9}$$

The grand thermodynamic potentials can be determined either by the Peterson–Gubbins method,[44] which implies auxiliary simulations at supercritical conditions, or by the gauge cell simulation method[32,33] employed in this work, which allows us to construct a continuous isotherm connecting vaporlike and liquidlike states generated in GCMC simulation.

C. Gauge cell MC simulation

In the gauge cell MC method,[32,33] the simulation is performed simultaneously in two cells, which are in chemical equilibrium at isothermal conditions. One of the cells represents the pore and the other is the gauge cell of a limited capacity. Mass exchange between the cells is allowed; however, the cell volumes are kept unchanged. The density fluctuations in the pore are controlled by the capacity of the gauge cell. In the limit of infinite capacity, the gauge cell method is equivalent to the grand canonical MC (GCMC) method. In the limit of vanishing capacity, it is equivalent to the canonical ensemble MC (CEMC) method. Choosing the ratio of the gauge cell and pore volumes sufficiently small, one can stabilize the fluid in the pore cell in a state, which would be unstable during the contact with the bulk. Thus, the gauge cell has two functions: to prevent undesirable growth or decay of nuclei, and to measure the chemical potential of the pore fluid.

The results of the gauge cell simulation are presented in Fig. 1 by open circles. Combining the results of the GCMC and gauge cell methods we constructed a continuous, van der Waals-type isotherm of confined fluid. It is worth noting that the states generated in GCMC and in the gauge cell method overlap with a remarkable accuracy. The combined isotherm is equivalent to the isotherm that would be obtained in the canonical NVT ensemble with a continuous variation of the number of molecules in the system and the chemical potential determined by the Widom formula[45] as

$$\mu_{\mathrm{CE}}(N)=F(N+1,V,T)-F(N,V,T)\approx\left.\frac{\partial F(N,V,T)}{\partial N}\right|_{V,T}. \tag{10}$$

It should be noted that the direct application of the Widom method for determining the chemical potential in the NVT simulation is not feasible with a required accuracy due to a highly inhomogeneous structure of the fluid.[42] This is why the gauge cell method comes forefront in simulations of phase transitions in small systems.[32,46–48] The rigorous statistico-mechanical foundation of the gauge cell method and comparison with the particle insertion method will be presented elsewhere.

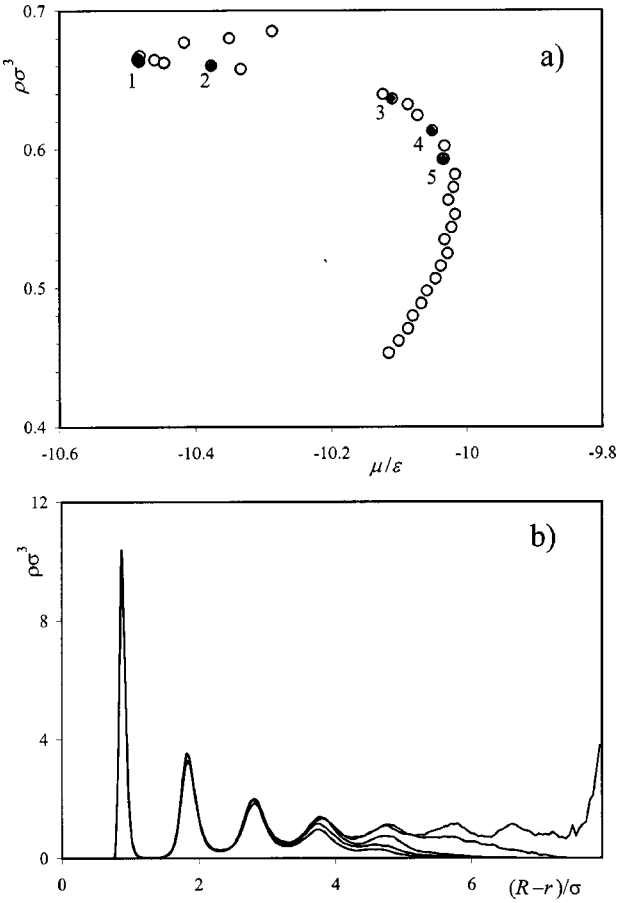

FIG. 2. (a) Metastable and unstable states of LJ fluid in 15.8σ pore at $kT/\epsilon=0.762$ obtained using the gauge cell method. The liquidlike spinodal (1) and bubble states (2–5) were equilibrated in additional long-run CEMC simulation. (b) Local density profiles for the liquidlike spinodal (1) and bubble states (2–5) marked in (a).

The gauge cell method allowed us to continue the GCMC isotherms of the vaporlike and liquidlike states up to the very spinodals. The vaporlike spinodal S_V represents the limit of metastability of adsorption films and, respectively, vaporlike states. The liquidlike spinodal S_L represents the limit of metastability of the stretched condensed fluid. The spinodals are connected by the backward trajectory of labile states of negative compressibility, $N_b(\mu)$. These states, which are of our primary interest, correspond to bubbles, which would be subject to collapse if the constraints on density fluctuations were removed. These bubbles represent the critical nuclei of cavitation in the metastable liquidlike state being kept at the given chemical potential at the grand canonical ensemble conditions.

We are specifically interested in the vicinity of the liquidlike spinodal S_L enlarged in Fig. 2(a) since these bubbles represent critical nuclei of cavitation. The density profiles for five selected states marked in Fig. 2(a) are given in Fig. 2(b).

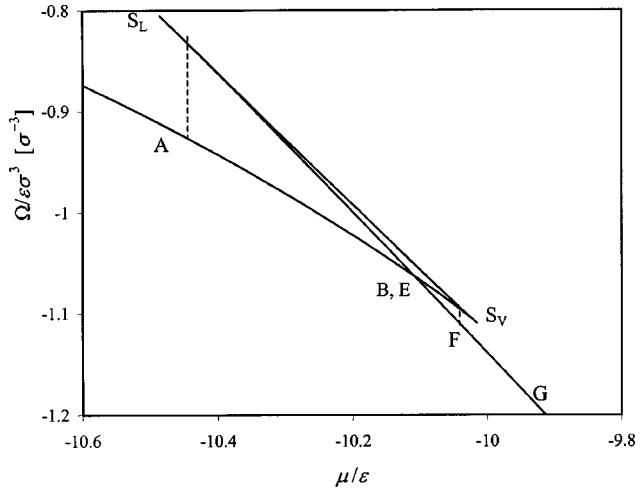

FIG. 3. Grand thermodynamic potential of the fluid (related to the pore volume) obtained by thermodynamic integration of the adsorption isotherm. For denotations (points B, C... etc.) see Fig. 1. Vertical dashed lines show the locations of capillary condensation and evaporation transitions observed in GCMC simulation.

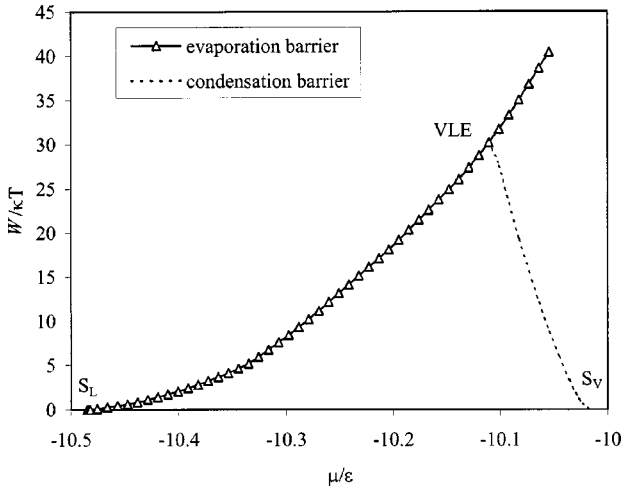

FIG. 4. Nucleation barrier for evaporation of LJ fluid in 15.8σ spherical pore at $kT/\epsilon=0.762$, which corresponds to the work of critical bubble formation. The nucleation barrier for capillary condensation equals the nucleation barrier for evaporation at VLE.

To provide the best statistics feasible, these states were equilibrated in the canonical ensemble within 15 mln MC steps. Going along the descending isotherm of labile states from the liquidlike spinodal (point 1), we monitor the formation of the bubble, which is located at the pore center due to the symmetry of the system. Microscopic features of the evolution of bubble configurations is analyzed below in Sec. III.

D. Nucleation barriers

The continuity of the constructed isotherm makes the calculation the grand thermodynamic potential, $\Omega(\mu,T)=F(N(\mu),T)-\mu N(\mu)$, possible by thermodynamic integration along the isotherm starting from a reference ideal gas state at a sufficiently low vapor pressure, $\Omega(\mu_r,T)=-kN_rT$

$$\Omega(\mu,T)-\Omega(\mu_r,T)=-\int_{(\mu_r)}^{(\mu)}N(\mu,T)d\mu. \tag{11}$$

The plot of the grand thermodynamic potential for vaporlike, liquidlike, and bubble states is given in Fig. 3. The point of intersection of vapor and liquid branches corresponds to the condition (8) of VLE. The chemical potential of VLE, μ_e, is thus determined using the Maxwell rule of equal areas cut off by the dashed vertical line BF in Fig. 1

$$\oint_{\mu}Nd\mu=0. \tag{12}$$

The equilibrium chemical potential found by the Maxwell rule, $\mu_e=-10.096\epsilon$ (for nitrogen at 77.4 K this corresponds to $p_e=0.346$ atm), agrees with the result, $\mu_e=-10.12\epsilon$, of the thermodynamic integration method of Peterson and Gubbins[44] that demonstrates a consistency of our method. In order to implement the Peterson–Gubbins method, a supercritical GCMC isotherm at $kT/\epsilon=1.38$ and a constant chemical potential path at $\mu=-9.0\epsilon$ were generated. The bubble branch located between the spinodals lie above the vapor and liquid branches. The grand potential difference between the bubble and liquidlike state at the given chemical potential represents the nucleation barrier for cavitation, $W_b(\mu)$, in accord with definition (4). The nucleation barrier is presented in Fig. 4. It increases rapidly as the bubble grows. At the liquidlike spinodal the nucleation barrier of cavitation diminishes, showing the limit of stability of stretched liquid. In Fig. 4, we also present the estimate of the nucleation barrier for vapor condensation calculated as the grand potential difference between the bubble and vapor state, $W_c(\mu)=\Omega_b(\mu,V,T)-\Omega_v(\mu,V,T)$. Being zero at the vapor spinodal, $W_c(\mu)$ intersects $W_b(\mu)$ at the point of VLE.

E. Comparison with CNT

It is tempting to compare the nucleation barriers computed in MC simulation with the predictions of CNT given by Eq. (3). However, this comparison should be done with proper reservations to avoid misleading conclusions. First, from a rigorous standpoint, the bubble radius in Eq. (3) is the radius of tension determined by the Laplace equation (2) rather that the equimolar radius, which is defined through Eq. (6). The difference between the radius of tension and the equimolar radius can be appreciable for the small clusters so that the substitution of the radius of tension determined from the equation of state by the equimolar radius cannot be justified. Second, a correct choice of the numeric value of the surface tension γ is very important. To avoid fitting, we employed the value $\gamma=0.91\epsilon/\sigma^2$ for a planar interface obtained by interpolation of simulation data[28] for bulk LJ fluid with 5σ cutoff at $kT/\epsilon=0.7625$. For small bubbles the surface tension is size-dependent. The deviations between the simulation and theoretical results can be reduced by using the Tolman relation between the surface tension and the bubble radius.[49] However, this relation involves an additional unknown parameter, the Tolman length. Third, as shown in our earlier studies of capillary condensation in nanoscale pores,[50] interactions of confined fluid with solid walls essentially af-

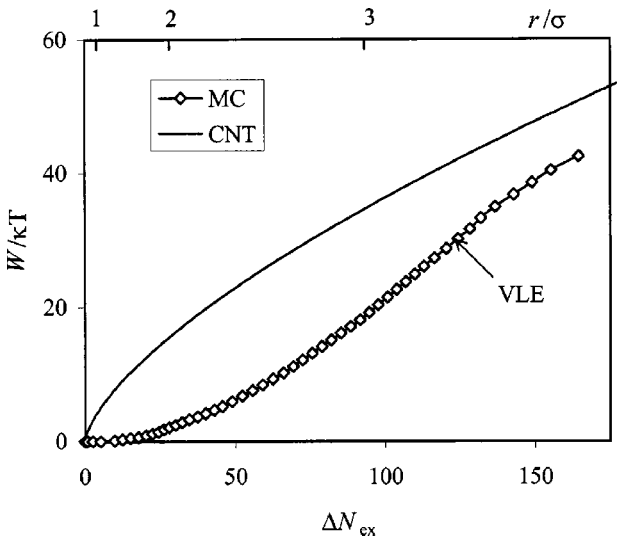

FIG. 5. Nucleation barrier calculated from MC isotherms using thermodynamic integration, Eqs. (4) and (11), as a function of the excess mass of the bubble N_{ex}, Eq. (5). CNT barriers were calculated from the MC excess isotherm N_{ex} in accord with Eqs. (3) and (7).

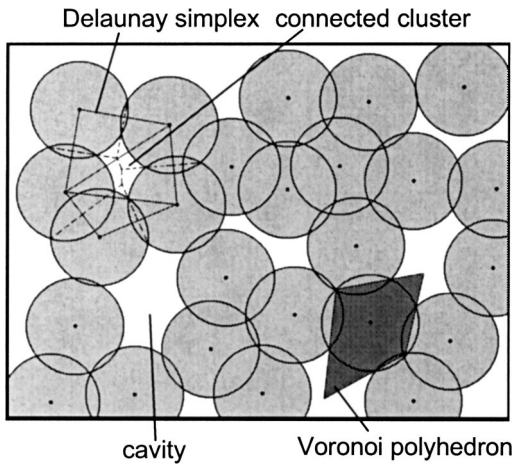

FIG. 6. Two-dimensional sketch describing Voronoi–Dalaunay tesselation. The shaded areas around each molecular center represent the occupied region. The void region (in white) correspond to disconnected intermolecular cavities.

fect the conditions of capillary equilibrium. In particular, due to a stabilizing action of wetting walls, the liquidlike spinodal is shifted to lower chemical potentials as compared to the liquid spinodal in the bulk fluid at the given temperature. For the LJ fluid considered in this work, the liquid spinodal according to the equation of Johnson *et al.*[51] (JZG) equals $\mu_{LS,bulk} \approx -10.34\epsilon$, while the liquidlike spinodal in 15.8σ silica pore is $\mu_{LS,bulk} \approx -10.48\epsilon$. Thus, we simulated bubble formation at the environmental conditions beyond the liquid spinodal that makes impossible to improve the CNT model by employing the JZG equation of state to determine the radius of tension via the Laplace equation (2).

Having in mind the above mentioned reservations, the only unequivocal way to compare MC and CNT is to plot the nucleation barrier W_b as a function of the excess bubbles mass N_{ex}, see Fig. 5. In so doing there is no ambiguity in presenting the MC data: both quantities are directly determined in simulation and fulfill the nucleation theorem, Eq. (6). The CNT prediction was calculated using Eq. (3) with the bubble radius determined from the given N_{ex} via Eq. (7) with the liquid and vapor densities of coexisting bulk phases at the given temperature. The equimolar radius related to the bubble excess mass through Eq. (7) is given on the upper axis of the graph. CNT severely overestimates the nucleation barrier for small bubbles. As the bubble size increases, the relative deviation becomes smaller.

III. STATISTICAL GEOMETRY OF CAVITATION

To study microscopic mechanisms of the bubble formation, we analyze the statistical geometry of intermolecular cavities. For a given configuration of molecules, a cavity is defined as a connected region where there is sufficient space to accommodate an additional molecule. This approach has been successfully employed in studies of metastability and phase transitions in bulk fluids, since valuable insight into the thermodynamic properties of model fluids was gained from studying the statistical geometry of cavity distributions.[15,35–37] In particular, bubble cavitation in superheated LJ liquid was studied by Corti and Debenedetti[52,53] and recently by Punnathanam and Corti.[10,54,55] The authors[52,53] introduced a void-constraint ensemble, where limits were imposed on the maximum size of cavities that were allowed to form. A statistical analysis of the cavity volume distribution was performed to determine when the constrains lead to unphysical results. The authors[10] found that the bubble cavitation is related to the formation of a critical cavity. Vishnyakov, Debenedetti, and Neimark[37] studied instability of a metastable stretched fluid confined to a slit-shaped pore. The onset of spontaneous evaporation was associated with the coalescence and growth of intermolecular cavities. Below, we apply similar ideas to understand the physical scenario of cavitation.

We exploit the technique introduced by Sastry *et al.*[35,36] for dense sphere packing, which was adopted to confined LJ fluid in our earlier work.[37] The method is based on the Voronoi-Delaunay tessellation technique applied to the configurations of molecular centers generated in MC simulation. The tessellation algorithms were taken from Ref. 34. To analyze the geometry of intermolecular cavities in a given configuration of molecules sampled in MC simulation, the simulation cell is divided into occupied and void regions. The occupied region is composed of exclusion spheres built around each molecular center. A two-dimensional sketch describing the definition of intermolecular voids is presented in Fig. 6. The radius of the exclusion sphere is chosen from the condition that the probability of insertion of an additional molecule, the center of which lies within the exclusion sphere, is vanishingly small. For LJ fluid considered here, the radius of the exclusion sphere was set equal to σ. The void region is composed of disconnected cavities. By definition, two points belong to the same cavity if there exists a continuous path in the void region connecting these points. The cavities have an irregular shape and are characterized by their volume and surface area.

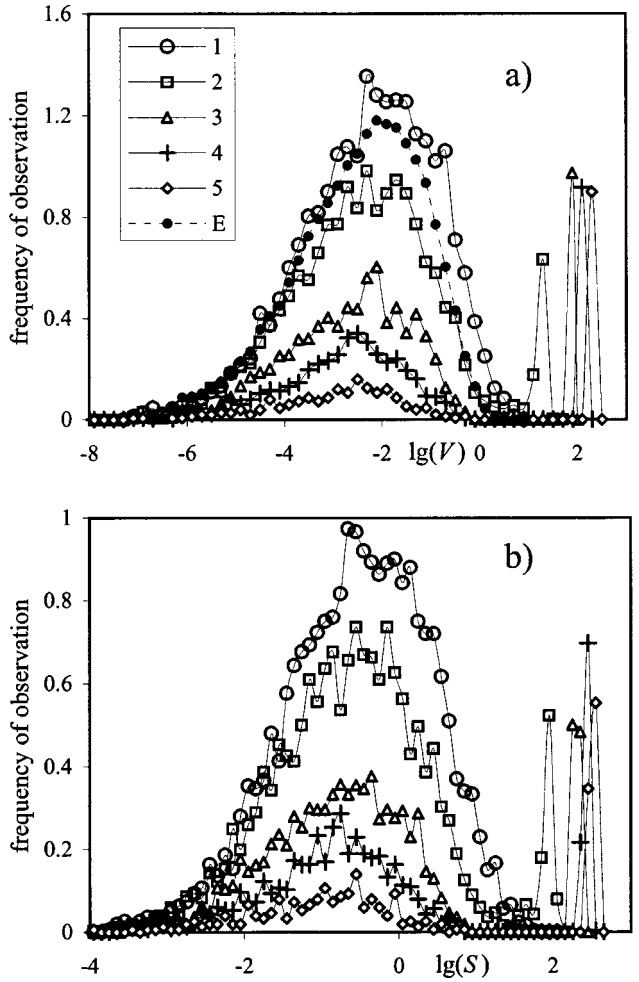

FIG. 7. Volume (a) and surface area (b) distributions of cavities for the liquidlike equilibrium (E), spinodal (1) and bubble states (2–5) denoted in Fig. 2.

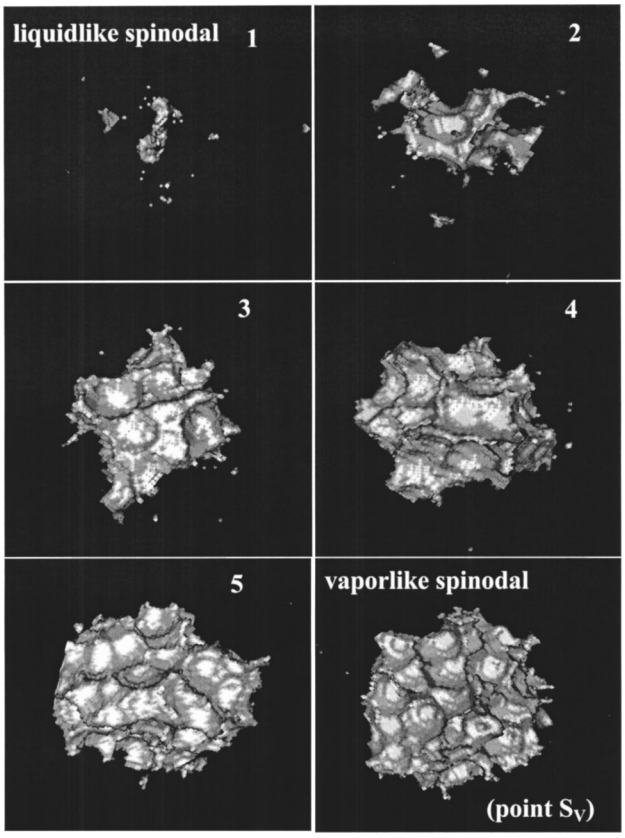

FIG. 8. Snapshots of bubbles surrounded by interstitial cavities.

Using the algorithm developed earlier in Refs. 34–36, we computed the distributions of volumes and surface areas of cavities in selected liquidlike states, liquidlike spinodal (point 1) and bubble states (2–5) indicated in Fig. 2(a). To provide a reliable statistics about $1.5*10^7$ configurations were generated in the canonical ensemble for each state point. The Voronoi–Delaunay tessellation and the cavity analysis was performed for molecular configurations obtained every 10^4 MC steps. Thus, statistics on the cavities was collected over 1500 configurations for each state point.

In Figs. 7(a) and 7(b) we present the distributions of cavity volumes and surface areas, respectively. The cavity distribution in the liquidlike state F (Fig. 1) near VLE has a skewed log-normal shape typical for interstitial cavities. The volume distribution spans over seven decimal decades. The largest interstitial cavities sampled in minute quantities do not exceed 1 σ in diameter and the most probable size, which corresponds to the maximum of the distribution is about 0.1 σ. As the fluid density decreases, the void density and accordingly the number and dimensions of cavities increase. This is seen from the comparison of the cavity distributions at the liquidlike spinodal S_L (curves 1) and at VLE (curve E). For states 2–5, the cavity distribution possesses the second peak, which indicates the appearance of cavities of size of few σ. The location of the second peak is shifted to larger sizes as the fluid density decreases. These large cavities correspond to the bubble, whose size fluctuates from configuration to configuration. Selected snapshots of cavities are presented in Fig. 8. The cavities, which are the results of the Voronoi–Delaunay tessellation, have rough surface with pronounced bowl-shaped imprints from bounding exclusion spheres. As the fluid density decreases from states 1 to 5 we observe the large growing cavity located around the cell center surrounded by smaller interstitial cavities. This cavity is a momentary replica of a certain configuration of the bubble, which upon averaging over sampled configurations has a spherical shape. The density profiles of these states are given in Fig. 2(b).

As the bubble grows, the distribution of interstitial cavities depletes as seen from Fig. 7. This means that the bubble grows at the expense of interstitial cavities. The liquid layer around the bubble consolidates, and its density increases, which corresponds to the increase of the chemical potential. Remarkably, the distribution of interstitial cavities remains self-similar: Plotted in reduced coordinates, the distributions of interstitial cavities for all states collapse on a universal curve (Fig. 9) Similar universal behavior was found for confined metastable fluid in Ref. 37. In Fig. 10, we show the surface-to-volume scaling relation for cavities sampled in different states. The plots confirm that the cavity surface area scales with volume according to 2/3 power law characteristic to nonfractal three-dimensional objects, $S \sim V^{2/3}$. The cavity shape factor $g = S/V^{2/3}$ is about 10. The shape factor g re-

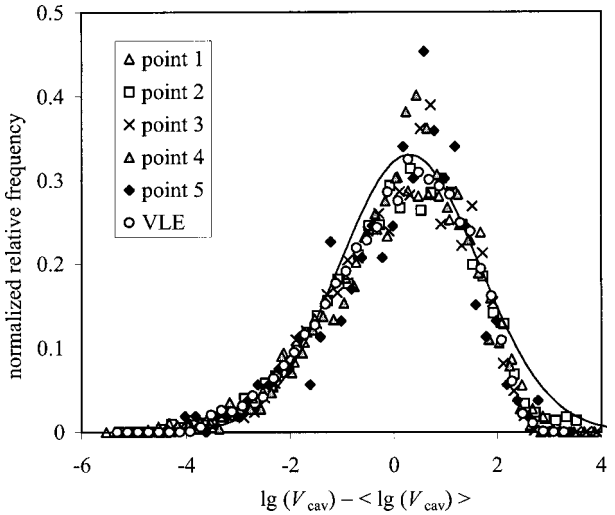

FIG. 9. Self-similarity of the distribution of interstitial cavities. Cavity distributions in reduced coordinates colapse on a universal curve. A log-normal distribution shown by a solid line is a guide for the eye.

flects the surface-to-volume ratio for the object of unit volume; for spheres $g=4.83$, for cubic cavities $g=6.0$, for tetrahedra $g=7.20$. Thus, interstitial cavities are irregular three-dimensional objects with a jagged surface. Formation of the bubble is displayed by the appearance of a group of points in the region of larger volumes, which are separated from the interstitial cavities. It is truly amazing that the surface-to-volume scaling relation for bubbles is the same as for interstitial cavities despite a significant gap in sizes: The points corresponding to bubbles and interstitial cavities lie on the same straight line.

It is worth noticing that the distributions of cavities for the states equilibrated within different statistico-mechanical ensembles are indistinguishable. A prominent example of the cavity distributions determined in GCMC, CEMC, and gauge cell MC methods is given in Fig. 7(c).

IV. COMPARISON WITH EXPERIMENT

To compare simulation results with real experiments, we have intentionally chosen for simulation the system which mimics the nitrogen sorption in silica pores at nitrogen normal boiling temperature. The experimental isotherm measured on a sample of HMM-3 type ordered mesoporous molecular sieve of with Pm3n cubic symmetry[39] is given in Fig. 11. This sample, whose symmetry is confirmed by independent electron microscopy studies,[39] possesses a regular array of spheroidal pores with the averaged diameter of about 5.54 nm[31] corresponding to 15.8 The experimental isotherm is reversible in contrast to the ''practical'' hysteretic GCMC isotherm (Fig. 1) simulated at the conditions, which imitate the experimental ones, i.e., open system in equilibrium with an infinite reservoir. Practical means that the simulation run was finite and the sampling was confined to the basins of vaporlike and liquidlike states, which are separated by the nucleation barrier at VLE. The value of the nucleation barrier at VLE, $W_b(\mu)=W_c(\mu)=31.4\,\mathrm{kT}$, determines the probabil-

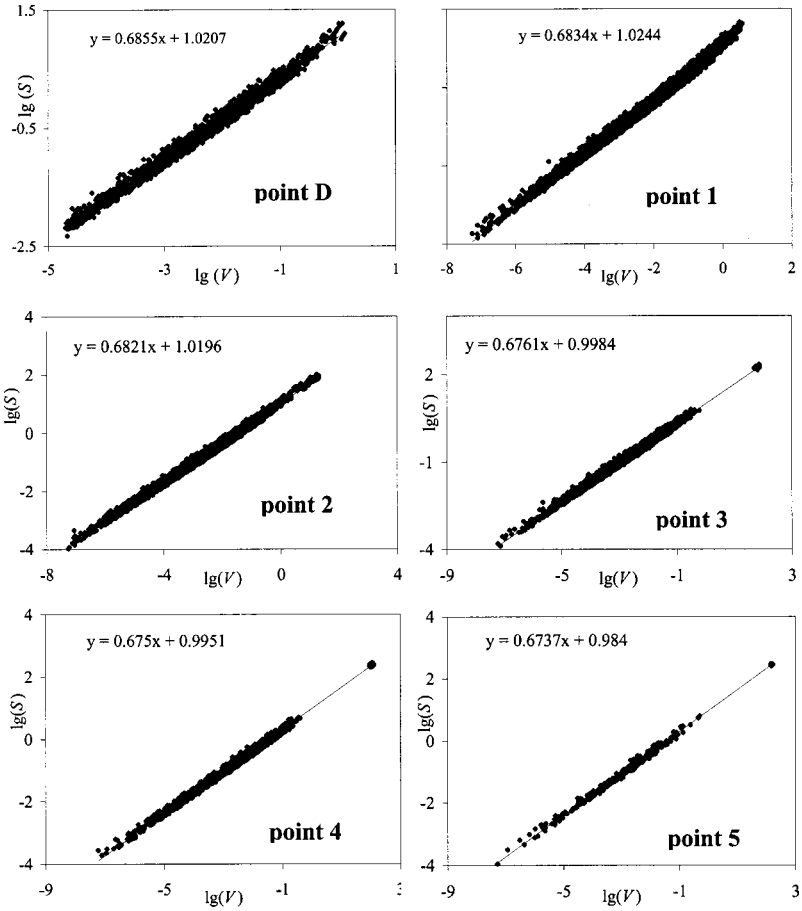

FIG. 10. Volume-to surface area relation for intermolecular cavities in different states. D-metastable liquidlike state of spontaneous desorption (see Fig. 1), 1-liquidlike spinodal, 2–5-bubble states (see Fig. 2).

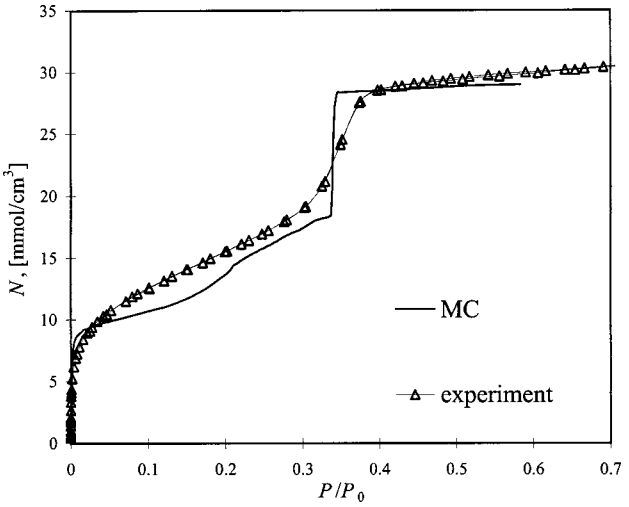

FIG. 11. Experimental adsorption isotherm of nitrogen at nitrogen boiling temperature of 77.4 K on a sample of HMM-3 material with Pm3n cubic symmetry with nominal diameter of spheroidal pores of 5.54 nm (Refs. 31 and 39) and calculated MC isotherm for LJ model nitrogen in the spherical silica pore of 15.8 σ.

ity of the equilibrium vapor–liquid transition in the system under consideration at the grand canonical ensemble conditions. This barrier is obviously too high for practical GCMC simulation runs even as long as 10^7 MC cycles. In our simulation, the barriers, which were overcome during spontaneous condensation (C→F) and evaporation transitions (D→A), were equal to 8.4 and 2.6 kT, respectively. However, in real experiments with metastable cryogenic liquids, the nucleation barriers smaller then ~70 kT corresponds to explosive boiling.[5] Thus, it is not surprising that capillary condensation isotherms measured in such small pores exhibit a prominent step, which is reproduced in the reverse process of evaporation without hysteresis.

At the same time, we find excellent agreement of the experimental isotherm with the ''true'' GCMC isotherm constructed by connecting the vapor and liquid branches by the VLE step, Fig. 11. This isotherm (i.e., combined isotherm ABFG in Fig. 1) would be obtained in truly unconstrained GCMC simulation with ''infinite'' number of MC cycles that would make sampling the whole configuration space possible. The position of the capillary condensation step is reproduced accurately: The inflection point of the experimental isotherm practically coincides with the VLE transition predicted in simulation. The condensed fluid density is predicted within few % (a quantitative comparison is hindered due to an inherent pore size distribution which, for this sample, is narrow yet not negligible). Although the qualitative trend of the isotherm in the region of monolayer and multilayer adsorption (vaporlike states) is captured correctly, there are noticeable deviations, which are attributed to a natural energetic heterogeneity and molecular roughness of silica surface. It is worth noticing that no adjustable parameters were employed in the simulation model; the parameters for fluid–fluid and fluid–solid intermolecular potentials were taken from our earlier works[56] where they were found to reproduce the VLE for the bulk fluid and the isotherm on a nonporous surface.

V. CONCLUSIONS

We presented a comprehensive molecular simulation study of bubble formation in metastable LJ fluid confined to a spherical pore with wetting walls. The system parameters were chosen to imitate nitrogen at its normal boiling temperature adsorbed in pores of siliceous materials that made possible a comparison with experimental data. Different simulation methods were employed: GCMC method to generate stable and metastable vaporlike and liquidlike states, CEMC method to explore specifics of molecular configurations, and the gauge cell MC method to stabilize the states unstable in GCMC simulations and thus to construct a continuous van der Waals-type isotherm of confined fluid, Fig. 1. We showed that the backward branch of this isotherm corresponds to bubble states stabilized in the gauge cell method. Following the evolution of the bubble states along the constructed isotherm starting from the liquidlike spinodal, we investigated the birth of a bubble in the metastable stretched liquid and its growth. We assume that this process resembles the process of homogeneous cavitation.

The bubble sizes and nucleation barriers were calculated from a purely thermodynamic standpoint as excess quantities. The bubble size was defined from the excess isotherm, which is the difference between the loadings (total number of molecules) in the bubble state and in the liquid state at the same chemical potential. The nucleation barrier was defined as the difference between the grand thermodynamic potentials of these states. The continuity of the simulated isotherm made possible to obtain the nucleation barrier by direct thermodynamic integration. We found that the classical nucleation theory severely overestimated the nucleation barrier for small bubbles.

We applied the Voronoi–Delaunay tessellation technique to analyze the statistical geometry of molecular configurations in the process of cavitation. We showed that bubble formation can be considered as the process of coalescence of intermolecular cavities. The latter are defined as voids between the molecules is which additional molecule(s) can be inserted. The statistical analysis of the evolution of the population of interstitial intermolecular cavities confirmed the following scenario of the birth of a bubble in a stretched fluid. As the degree of metastability increases and the fluid becomes progressively stretched, the number and sizes of intermolecular cavities increases. At the spinodal, the fluid becomes mechanically unstable: Interstitial cavities partly coalesce into a larger cavity located due to the system symmetry around the pore center. This cavity represents a bubble embryo, which grows at the expense of interstitial cavities into a critical nucleus. We found that the distribution of interstitial cavities remains self-similar disregarding the fluid density. The surface-to-volume ratio for interstitial cavities obeys the three-dimensional scaling, $S \sim V^{2/3}$ over the seven orders of magnitude.

The results of simulation were compared with the nitrogen adsorption isotherm measured at 77.4 K on a sample of HMM-3 siliceous mesoporous molecular sieve, which contained an array of spheroidal pores of average size of 5.54 nm. We found that the experimental isotherm, which is reversible, in contrast with the CGMC simulated hysteretic iso-

therm, agrees quantitatively with the theoretical isotherm, which would be obtained in ''truly'' unconstrained GCMC simulation with an ''infinite'' number of simulation steps. That is the nucleation barrier of about 30 kT which was determined for the system under consideration here, was insurmountable in practical GCMC simulations with several millions simulation steps. At the same time, this barrier did not obstruct condensation and evaporation transitions in real experiments with characteristic equilibration time of several minutes and inherent fluctuations of environmental conditions, temperature, and pressure.

Although the effects of confinement in the model system we considered here are not by any means negligible and the interaction with solid walls represents an additional stabilizing factor, we are inclined to believe that the observed scenario of bubble formation via coalescence of interstitial cavities captures major features of homogeneous nucleation. It is worth noting that this scenario correlates with the studies of Punnathanam and Corti[10,53,54] of cavity formation in the process of bubble nucleation in the superheated LJ fluid. The estimate of nucleation barriers by direct integration along the continuous isotherm generated by means of the gauge cell method sheds light on the origin of the capillary condensation hysteresis observed in larger pores. The hysteresis should be expected when the nucleation barrier, which is a progressively increasing function of the pore size, becomes insurmountable at given experimental conditions.

ACKNOWLEDGMENTS

The work is supported by the TRI/Princeton exploratory research program. A.V.N. thanks the John Simon Guggenheim Memorial Foundation for a 2004 Guggenheim Fellowship.

[1] V. P. Skripov, *Metastable Liquids* (Wiley, New York, 1974).
[2] P. G. Debenedetti, *Metastable Liquids: Concepts and Principles* (Princeton University Press, Princeton, 1996).
[3] D. Gardellin, Chem. Eng. Prog. **92**, 52 (1996).
[4] Y. L. Chen and J. Israelachvili, Science **252**, 1157 (1991).
[5] V. G. Baidakov, *Overheated Cryogenic Liquids* (RAN, Ekaterinburgh, 1995).
[6] S. J. Putterman, Sci. Am. **272**, 46 (1995).
[7] B. Niemczewski, Trans. Inst. Met. Finish. **81**, 28 (2003).
[8] E. Maisonhaute, C. Prado, P. C. White, and R. G. Compton, Ultrason. Sonochem. **9**, 297 (2002).
[9] J. W. Gibbs, *The Scientific Papers of J. Willard Gibbs* (Dover, New York, 1961).
[10] S. Punnathanam and D. S. Corti, Phys. Rev. E **69**, 036105 (2004).
[11] V. G. Baidakov and S. P. Protsenko, Dokl. Phys. **49**, 69 (2004).
[12] J. W. P. Schmelzer, V. G. Baidakov, and G. S. Boltachev, J. Chem. Phys. **119**, 6166 (2003).
[13] Y. W. Wu and C. Pan, Microscale Thermophys. Eng. **7**, 137 (2003).
[14] H. Okumura and N. Ito, Phys. Rev. E **67**, 045301 (2003).
[15] V. K. Shen and P. G. Debenedetti, J. Chem. Phys. **118**, 768 (2003).
[16] C. Xiao, D. M. Heyes, and J. G. Powles, Mol. Phys. **100**, 3451 (2002).
[17] S. H. Park, J. G. Weng, and C. L. Tien, Int. J. Heat Mass Transfer **44**, 1849 (2001).
[18] T. Kinjo, G. T. Gao, and X. C. Zeng, Prog. Theor. Phys. Suppl. **138**, 732 (2000).
[19] M. Blander and J. L. Katz, AIChE J. **21**, 833 (1975).
[20] I. Kusaka and D. W. Oxtoby, J. Chem. Phys. **110**, 5249 (1999).
[21] D. W. Oxtoby, J. Phys.: Condens. Matter **4**, 7627 (1992).
[22] D. W. Oxtoby and R. Evans, J. Chem. Phys. **89**, 7521 (1988).
[23] X. C. Zeng and D. W. Oxtoby, J. Chem. Phys. **94**, 4472 (1991).
[24] Y. Viisanen, R. Strey, and H. Reiss, J. Chem. Phys. **99**, 4680 (1993).
[25] D. Kashchiev, J. Chem. Phys. **76**, 5098 (1982).
[26] A. I. Rusanov and E. N. Brodskaya, J. Colloid Interface Sci. **62**, 542 (1977).
[27] P. R. tenWolde and D. Frenkel, J. Chem. Phys. **109**, 9901 (1998).
[28] B. Chen, J. I. Siepmann, K. J. Oh, and M. L. Klein, J. Chem. Phys. **115**, 10903 (2001).
[29] K. Morishige, N. Tateishi, and S. Fukuma, J. Phys. Chem. B **107**, 5177 (2003).
[30] P. I. Ravikovitch and A. V. Neimark, Langmuir **18**, 9830 (2002).
[31] P. I. Ravikovitch and A. V. Neimark, Langmuir **18**, 1550 (2002).
[32] A. Vishnyakov and A. V. Neimark, J. Phys. Chem. B **105**, 7009 (2001).
[33] A. V. Neimark and A. Vishnyakov, Phys. Rev. E **62**, 4611 (2000).
[34] M. Tanemura, T. Ogawa, and N. Ogita, J. Comput. Phys. **51**, 191 (1983).
[35] S. Sastry, P. G. Debenedetti, and F. H. Stillinger, Phys. Rev. E **56**, 5533 (1997).
[36] S. Sastry, T. M. Truskett, P. G. Debenedetti, S. Torquato, and F. H. Stillinger, Mol. Phys. **95**, 289 (1998).
[37] A. Vishnyakov, P. G. Debenedetti, and A. V. Neimark, Phys. Rev. E **62**, 538 (2000).
[38] A. V. Neimark, P. I. Ravikovitch, and A. Vishnyakov, Phys. Rev. E **62**, R1493 (2000).
[39] S. Inagaki, S. Guan, Y. Fukushima, T. Ohsuna, and O. Terasaki, J. Am. Chem. Soc. **121**, 9611 (1999).
[40] A. Vishnyakov and A. V. Neimark, Langmuir **19**, 3240 (2003).
[41] P. I. Ravikovitch, A. Vishnyakov, and A. V. Neimark, Phys. Rev. E **64**, 011602 (2001).
[42] D. Frenkel and B. Smit, *Understanding Molecular Simulation. From Algorithms to Applications* (AP, San Diego, 1996).
[43] G. E. Norman and V. S. Filinov, High Temp. **7**, 216 (1969).
[44] B. K. Peterson and K. E. Gubbins, Mol. Phys. **62**, 215 (1987).
[45] B. Widom, J. Chem. Phys. **39**, 2808 (1963).
[46] J. W. Jiang, S. I. Sandler, and B. Smit, Nano Lett. **4**, 241 (2004).
[47] M. Jorge and N. A. Seaton, Mol. Phys. **100**, 3803 (2002).
[48] A. Vishnyakov and A. V. Neimark, J. Chem. Phys. **119**, 9755 (2003).
[49] R. C. Tolman, J. Chem. Phys. **17**, 333 (1949).
[50] A. V. Neimark, P. I. Ravikovitch, and A. Vishnyakov, J. Phys.: Condens. Matter **15**, 347 (2003).
[51] J. K. Johnson, J. A. Zollweg, and K. E. Gubbins, Mol. Phys. **78**, 591 (1993).
[52] D. S. Corti and P. G. Debenedetti, Ind. Eng. Chem. Res. **34**, 3573 (1995).
[53] D. S. Corti and P. G. Debenedetti, Chem. Eng. Sci. **49**, 2717 (1994).
[54] S. Punnathanam and D. S. Corti, Ind. Eng. Chem. Res. **41**, 1113 (2002).
[55] S. Punnathanam and D. S. Corti, J. Chem. Phys. **120**, 11658 (2004).
[56] P. I. Ravikovitch, A. Vishnyakov, R. Russo, and A. V. Neimark, Langmuir **16**, 2311 (2000).